Supporting Information

The promotion of nitrate conversion into ammonia via the construction of tandem dual active sites of copper and cuprous oxide

Yujiao Wang, Zhiman Bai,* Kun Huang, Shan Wang, Fusheng Wang, Mingzai Wu*

School of Materials Science and Engineering, Key Laboratory of Photoelectric Conversion Energy Materials and Devices of Anhui Province, Anhui university, Hefei 230601, China.

E-mail: wumz@ahu.edu.cn, baizhiman@ahu.edu.cn

Experimental Procedures

Chemicals and materials

Sodium hydroxide (NaOH, ≥96.0%), Sodium sulfate anhydrous (Na_2SO_4,99%) ammonium sulfate-^{14}N ($(^{14}NH_4)_2SO_4$, 98.5%), ammonium sulfate-^{15}N ($(^{15}NH_4)_2SO_4$, ≥99 at%, 98.5%), sodium nitrate-^{14}N ($Na^{14}NO_3$, ≥99%), sodium nitrate-^{15}N ($Na^{15}NO_3$,$^{15}N \geq 99$ at%, 98.5%), maleic acid ($C_4H_4O_4$, ≥99.0%), deuterium oxide (D_2O, 99 at% D), DL-Lactic acid ($C_3H_6O_3$, ≥85%), Copper sulfate pentahydrate ($CuSO_4 \cdot 5H_2O$, 99%). Ni foam (NF, pore density 120 PPI) was bought from Kunshan Guang jia yuan New Material Co., Ltd. Milli-Q water (18.25 MΩ cm^{-1}) was used in all the experiments.

Preparation of Ni-Cu/Cu_2O.

0.4 M $CuSO_4$-$5H_2O$, 8.5% lactic acid and NaOH (0.3 M) were used as deposition solution. The above solution was added to the electrolytic cell and washed 1*1.5 cm^2 nickel foam was used as the working electrode, while the counter electrode and reference electrode were platinum sheet and silver chloride electrode, respectively. The electrodes were deposited with i-t at a voltage of -0.8 V (*vs*. RHE) for 5 min. Finally, the deposited samples were rinsed several times with deionised water and dried in a vacuum oven at 60 °C.

Preparation of Ni-Cu.

0.4 M $CuSO_4$-$5H_2O$ was dissolved in 30 ml of deionised water with stirring as the deposition solution, and the deposition method was consistent with Ni-Cu/Cu_2O.

Preparation of Ni foam.

The nickel foam of 1 × 1.5 cm^2 was cut and sonicated with hydrochloric, acetone, ethanol and water respectively for 20 min and finally dried in a 60 ^oC oven.

Materials Characterizations.

Powder X-ray diffraction (XRD) patterns were obtained using a Philips X'Pert PRO SUPER X-ray diffractometer equipped with graphite-monochromated Cu Kα radiation

(λ=1.54056 Å). The morphologies and elemental mapping analysis were identified by scanning electron microscopy (SEM Sigma 500, SEISS, Germany) and field emission transmission electron microscope (STEM, JEM-F200, JEOL) equipped with an energy dispersive spectrometer (EDS). X-ray photoelectron spectroscopy (XPS) measurements were carried out with an Escalab 250Xi system using a monochromatic Al Ka source (1,486.6 eV) for the analysis of the surface chemical property. The electron paramagnanetic resonance (EPR) measurements of DMPO-H were carried out at Bruker PLS-SXE300^{+}. The ultraviolet-visible (UV-Vis) absorbance spectra were measured on Shimadzu UV-3900 spectrophotometer. The isotope labeling experiments were measured by 1H NMR measurement (JNM-ECZ400R). The X-ray absorption fine structure (XAFS) measurements were carried out with the table XAFS-500A. The resulting XAFS data were analyzed using Demeter software.[1] The reaction intermediate information was studies by in Via Raman Microscope (RENISHAW, UK).

Electrochemical Measurements.

The electrochemical nitrate reduction reaction experiments were carried out in a single chamber 50 ml electrolytic cell using a standard three electrode system. Catalysts loaded on nickel foam and carbon paper, silver chloride reference electrode (Ag/AgCl) and catalyst on platinum foil were used as working, reference and counter electrodes, respectively. The reaction area of the working electrode was controlled to be 0.5 cm^2. The electrolyte was 0.5 M Na_2SO_4 solution and the target reactant was $NaNO_3$. The electrolyte was stirred at a rate of 500 revolutions per minute during the reaction. All electrochemical measurements were performed using an electrochemical workstation (CHI 660e, Zhenhua, Shanghai, China). Potentials were recorded at a standard hydrogen electrode with the conversion equation $E_{(RHE)} = E_{(Ag/AgCl)} + 0.059\ pH + 0.198$. Linear scanning voltammetry was carried out to bring the polarisation curves to a steady state prior to the nitrate electroreduction test. Constant potential tests were carried out for 1 h at different potentials. All LSV curves were performed between 0 V and -1.5 V versus RHE at a scan rate of 5 mV s^{-1}. EIS tests were performed in the frequency range of 100 KHz-0.1 Hz. C_{dl} values were evaluated by CV measurements in the potential

range without Faraday current density.

Zn-NO_3^- Battery Preparation

The electrochemical performance of the mixed liquid Zn-NO_3^- cell in a two-electrode system was determined in an H-cell. A one-piece (1 × 1 cm^2) Ni-Cu/Cu_2O cathode in 0.1 M $NaNO_3^-$/1 M KOH electrolyte and a Zn foil anode (1 × 1 cm^2) in 1 M KOH were separated by a Nafion NR211 membrane. All cell data were recorded in a CHI 660e electrochemical workstation.

N isotope labeling experiments.

Experiments on N isotope labelling were carried out by electrochemical nitrate reduction in electrolyte (0.1M NO_3^--N) using $Na^{15}NO_3$ and $Na^{14}NO_3$ as N sources, respectively.[2] For quantification, a series of standard solutions were prepared and standard curves were plotted. Firstly, a series of $^{15}NH_4^+$ solutions of known concentration mixed with 300 ppm maleic acid in 0.5 M Na_2SO_4 were prepared as standard solutions; secondly, 50 μL of deuterium oxide (D_2O) was added to the above mentioned 0.5 mL of mixed solution for NMR detection; finally, since the $^{15}NH_4^+$ concentration and the area ratio were positively correlated, $^{15}NH_4^+$ and maleic acid were utilised as the peak area ratio for calibration. Similarly, the amount of $^{14}NH_4^+$ was quantified in this way when using $Na^{14}NO_3$ as the feed N source. Due to the limited sensitivity of instrumental detection, this work has been tested with five-fold dilution of Na_2SO_4 following the reaction.

Ion concentration detection methods.

Nitrate, nitrite and ammonium concentrations were determined using a colourimetric method.[3] The ionic concentrations of the electrolytes before and after testing were measured using an ultraviolet-visible spectrophotometer (UV-Vis) after dilution to appropriate concentrations matching the range of the calibration curve:[4]

1.Determination of nitrate-N: Nitrate concentration was measured according to standard methods. First, an amount of electrolyte solution was removed from the electrolytic cell and diluted to 5 mL to bring it within the detection range. Then 0.2 mL

of 5 wt% amino sulphonic acid solution was added to the above solution and allowed to stand for 10 minutes at room temperature. Absorption spectra were tested using a UV-visible spectrophotometer and the intensity of absorption at wavelengths of 220 nm and 275 nm was recorded. The final absorbance value was calculated by the formula $A = A_{220nm} - 2A_{275nm}$. A calibration curve was plotted using a range of concentrations from 0 to 20 mg L^{-1}. Sodium nitrate used for plotting the calibration curve was pre-dried in an oven at 105-110°C for 2 hours.

2.Determination of nitrite-N: A mixture of p-aminobenzenesulfonamide (0.4 g), N-(1-naphthyl) ethylenediamine dihydrochloride (0.02 g), ultrapure water (5 mL), and phosphoric acid (1 mL, ρ = 1.70 g/mL) was used as a color developing reagent. An amount of electrolyte was removed from the electrolytic cell and diluted to 5 mL to reach the detection range. Then 0.1 mL of color reagent was added to the above 5 mL of solution and mixed thoroughly and left to stand for 20 minutes before recording the intensity of absorption at a wavelength near 540 nm. The concentration-absorbance curve was calibrated using a series of sodium nitrite standard solutions.

3.Detection of ammonium-N: The ammonia content of the solutions was quantified using the indophenol blue spectrometer method. A mixture of NaOH (0.4 g), sodium citrate (0.5 g), ultrapure water (10 ml) and salicylic acid (0.5 g) was used, labelled solution A. A mixture of sodium hypochlorite (0.625 ml) and ultrapure water (19.375 ml) was used, labelled solution B. A mixture of sodium nitroferricyanide (0.1 g) and ultrapure water (10 ml) was used, labelled Solution C. For colorimetric analysis, an amount of electrolyte was removed from the electrolytic cell and diluted to 2 mL to reach the detection range. Then 2 mL of solution A was added and mixed thoroughly, followed by 1 mL of solution B and 0.2 mL of solution C. After standing for 120 min, the intensity of absorption at a wavelength near 655 nm was recorded. Concentration-absorbance curves were plotted using a series of standard ammonium chloride solutions ranging from 0 to 20 mg L^{-1}.

H* detection using DMPO.

H* capture experiments were performed in electrolytes with and without NO_3^-. To ensure sufficient *H generation, the cathode area was set to 1 × 1 cm^2 and the electrolyte was set to 50 mL. After 20 min of reaction at a reduction potential of -1.1 V (*vs* RHE), 60 μL of the electrolyte was removed and mixed with 10 μL of DMPO, and then the mixture was transferred to a capillary tube for detection.

Calculation of the conversion, yield, selectivity, and Faradaic efficiency.

The NO_3^- conversion rate was calculated as follows:

$$NO_3^- \text{ conversion} = \Delta C_{NO3}^- / C_0 \times 100\% \quad (1)$$

The selectivity of the product can be calculated by:

$$NH_4^+ \text{ selectivity } (S_{NH4}^+) = C_{NH4}^+ / \Delta C_{NO3}^- \times 100\% \quad (2)$$

$$NO_2^- \text{ selectivity } (S_{NO2}^-) = C_{NO2}^- / \Delta C_{NO3}^- \times 100\% \quad (3)$$

The yield of NH_4^+(aq) was calculated using equation:

$$\text{Yield } NH_4^+ = (C_{NH4}^+ \times V) / (M_{NH4}^+ \times t \times m) \quad (4)$$

The Faradaic efficiency was calculated as follows:

$$\text{Faradaic efficiency} = (8F \times C_{NH4}^+ \times V) / (M_{NH4}^+ \times Q) \times 100\% \quad (5)$$

where C_{NH4}^+ is the concentration of NH_4^+(aq), C_{NO2-} is the concentration of NO_2^-(aq), ΔC_{NO3}^- is the concentration difference of NO_3^- before and after electrolysis, C_0 is the initial concentration of NO_3^-, V is the electrolyte volume, t is the electrolysis time, m is the mass of catalyst, *F* is the Faradaic constant (96485 C mol^{-1}), Q is the total charge passing the electrode.

Theoretical calculation model.

All the DFT calculations were conducted based on the Vienna Ab-inito Simulation Package (VASP).[5,6] The exchange-correlation effects were characterized by the Perdew-Burke-Ernzerhof (PBE) functional within the generalized gradient approximation (GGA) method.[7,8] The core-valence interactions were accounted by the

projected augmented wave (PAW) method.[9] The energy cutoff for plane wave expansions was set to 480 eV, and the 3×3×1 Monkhorst-Pack grid k-points were selected to sample the Brillouin zone integration. The vacuum space is adopted 15 Å above the surfaces to avoid periodic interactions. The structural optimization was completed for energy and force convergence set at 1.0×10^{-4} eV and 0.02 eV $Å^{-1}$, respectively.

The Gibbs free energy change (ΔG) of each step is calculated using the following formula:

$$\Delta G = \Delta E + \Delta ZPE - T\Delta S \quad (6)$$

where ΔE is the electronic energy difference directly obtained from DFT calculations, ΔZPE is the zero point energy difference, T is the room temperature (298.15 K) and ΔS is the entropy change. ZPE could be obtained after frequency calculation by:[10]

$$ZPE = \frac{1}{2}\sum h\nu i \quad (7)$$

And the TS values of adsorbed species are calculated according to the vibrational frequencies:[11]

$$TS = k_B T \left[\sum_{k} \ln\left(\frac{1}{1 - e^{-h\nu/k_B T}}\right) + \sum_{k} \frac{h\nu}{k_B T} \frac{1}{\left(e^{h\nu/k_B T} - 1\right)} + 1 \right] \quad (8)$$

Supporting Figures

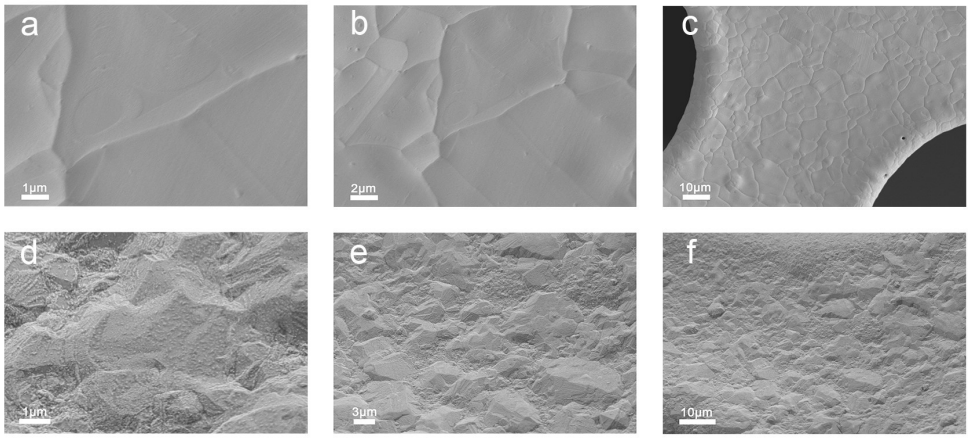

Fig. S1 (a-c) SEM images of Ni foam with different magnification. (d-f) SEM images of Ni-Cu with different magnification.

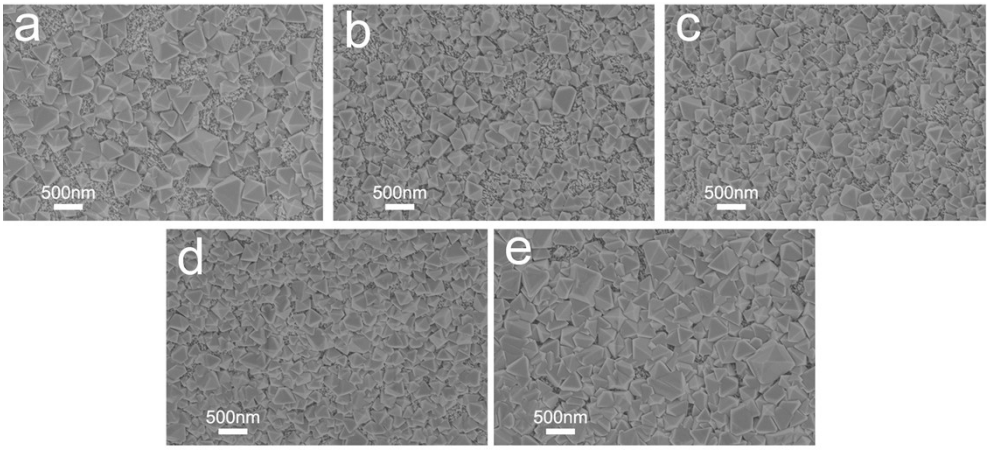

Fig. S2 SEM images of Ni-Cu/Cu_2O deposited at different voltages (a) -0.4 V, (b) -0.6 V, (c) -0.8 V, (d) -1.0 V, and (e) -1.2 V (*vs*. RHE).

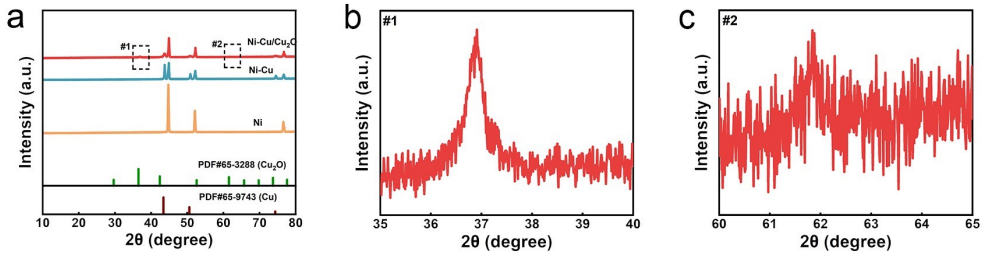

Fig. S3 XRD patterns of Ni-Cu/Cu_2O, Ni-Cu and Ni.

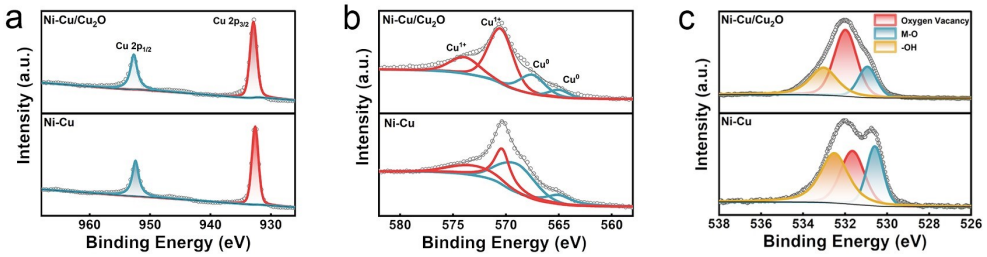

Fig. S4 Valence state characterizations of Ni-Cu/Cu_2O and Ni-Cu. (a) The Cu 2p high-resolution XPS (X-ray photoelectron spectroscopy) spectra of samples. (b) The Cu LMM auger XPS spectra of samples. (c) The O 1s high-resolution XPS spectra of samples.

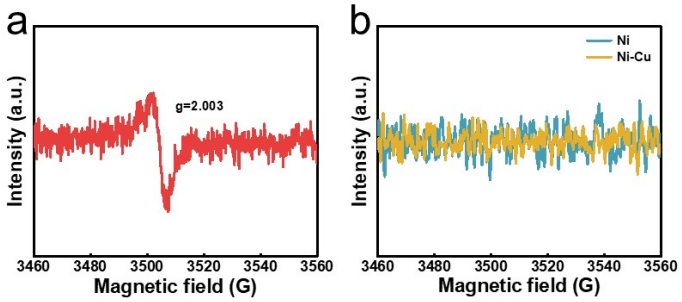

Fig. S5 The EPR spectra of (a) Ni-Cu/Cu_2O, (b) Ni-Cu and Ni.

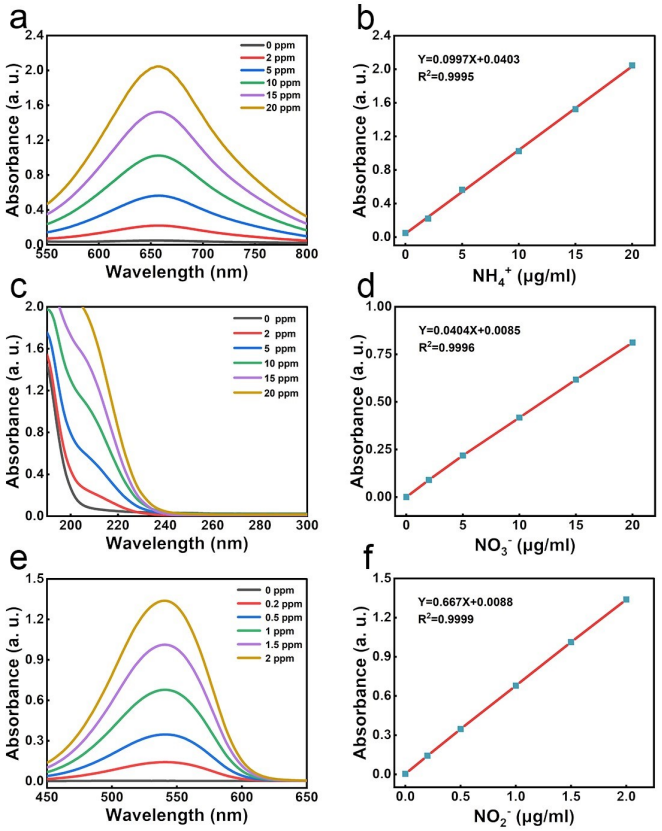

Fig. S6 Standard curves of concentration-absorbance of (a-b) NH_4^+, (c-d) NO_3^-, and (e-f) NO_2^- obtained by UV-vis spectroscopy method.

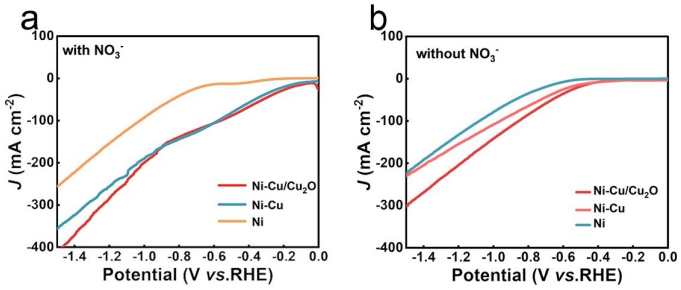

Fig. S7 The linear sweep voltammogram (LSV) curves of Ni-Cu/Cu_2O, Ni-Cu and Ni (a) with 0.1M NO_3^-, and (b) without NO_3^-.

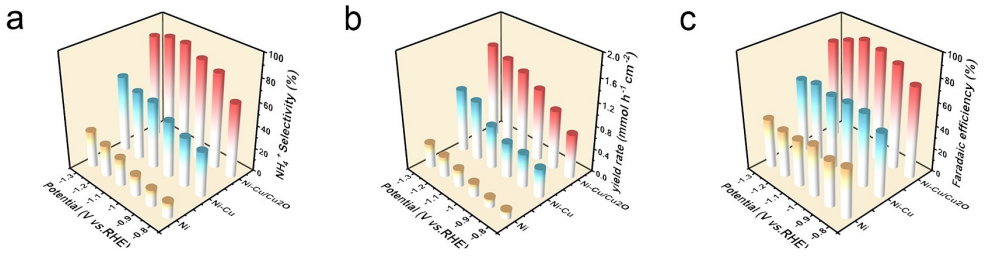

Fig. S8 The evaluation parameters of Ni-Cu/Cu_2O, Ni-Cu and Ni. (a) NH_4^+ selectivity. (b) yield rate of NH_4^+. (c) Faradaic efficiency of NH_4^+.

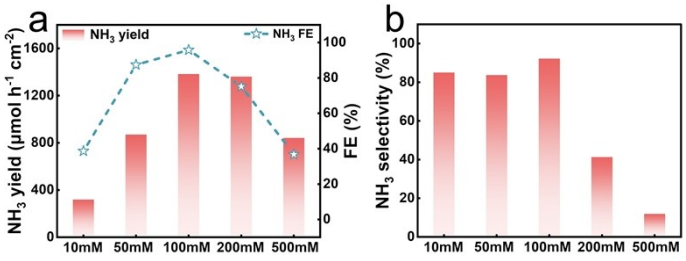

Fig. S9 Performance test of Ni-Cu/Cu_2O at different nitrate concentrations. (a) Ammonia Faraday efficiency and yield. (b) Ammonia selectivity.

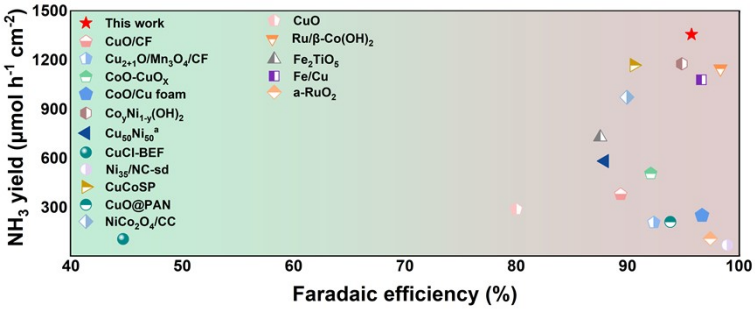

Fig. S10 Faraday efficiency and ammonium yield rate of Ni-Cu/Cu_2O are compared with reported electrocatalytic eNitRR based catalysts.

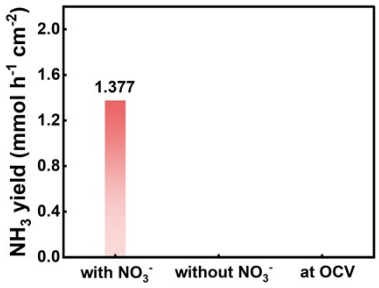

Fig. S11 Ammonium yield rate for Ni-Cu/Cu_2O in Na_2SO_4 electrolyte with NO_3^-, without NO_3^- and at OCV.

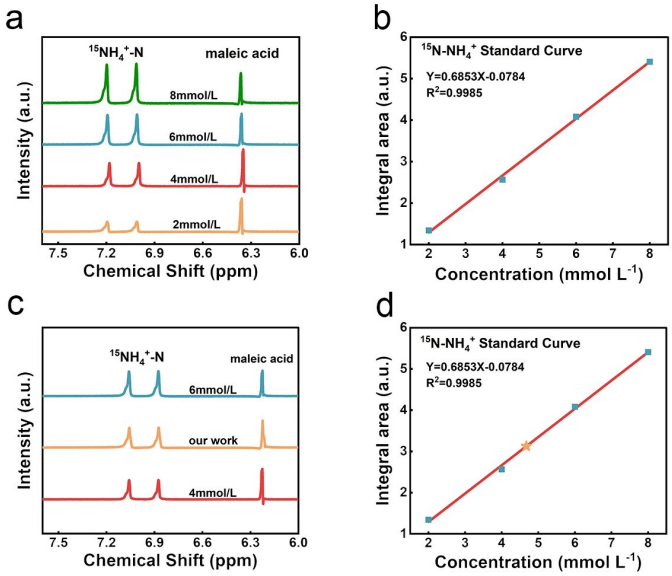

Fig. S12 (a) ^1H NMR spectra of various $^{15}NH_4^+$ ion concentration ($^{15}NH_4^+$-N) using maleic acid as reference (300 ppm). (b) Integral area ($^{15}NH_4^+$ / $C_4H_4O_4$) against $^{15}NH_4^+$ ion concentration ($^{15}NH_4^+$-N). (c) ^1H NMR spectra of the electrolyte after $^{15}NO_3^-$ reduction using Ni-Cu/Cu_2O at -1.1 V *vs*. RHE fdiluted fivefold for 1 h. (d) The $^{15}NH_4^+$ ion concentration ($^{15}NH_4^+$-N) of the electrolyte quantified by ^1H NMR using maleic acid (300 ppm) as reference.

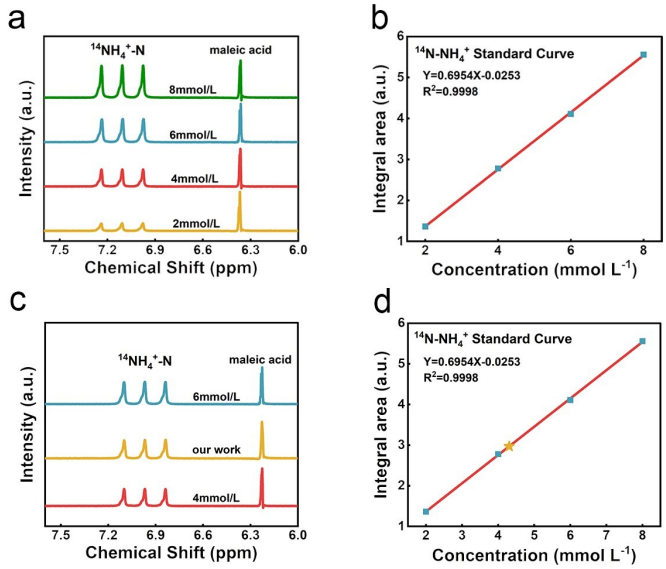

Fig. S13 (a) ^{1}H NMR spectra of various $^{14}NH_4^+$ ion concentration ($^{14}NH_4^+$-N) using maleic acid as reference (300 ppm). (b) Integral area ($^{14}NH_4^+$ / $C_4H_4O_4$) against $^{14}NH_4^+$ ion concentration ($^{14}NH_4^+$-N). (c) ^{1}H NMR spectra of the electrolyte after $^{14}NO_3^-$ reduction using Ni-Cu/Cu_2O at -1.1 V *vs*. RHE fdiluted fivefold for 1 h. (d) The $^{14}NH_4^+$ ion concentration ($^{14}NH_4^+$-N) of the electrolyte quantified by ^{1}H NMR using maleic acid (300 ppm) as reference.

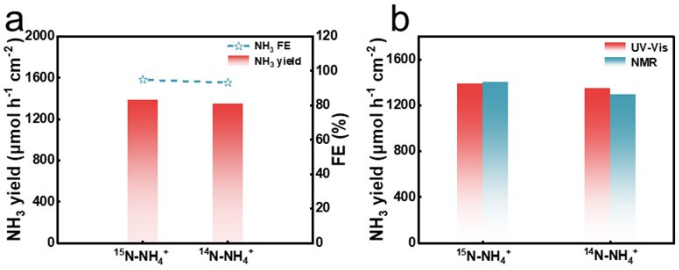

Fig. S14 (a) The comparison of ammonia yield and Faraday efficiency using $^{15}NO_3^-$-N and $^{14}NO_3^-$-N as sources. (b) the ammonia yield comparison detected by UV and NMR using $^{15}NO_3^-$-N and $^{14}NO_3^-$-N as sources.

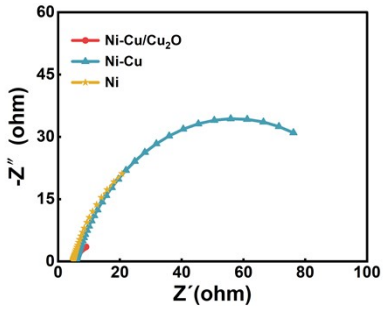

Fig. S15 The electrochemical impedance spectroscopy (EIS) measurements of Ni-Cu/Cu_2O, Ni-Cu and Ni.

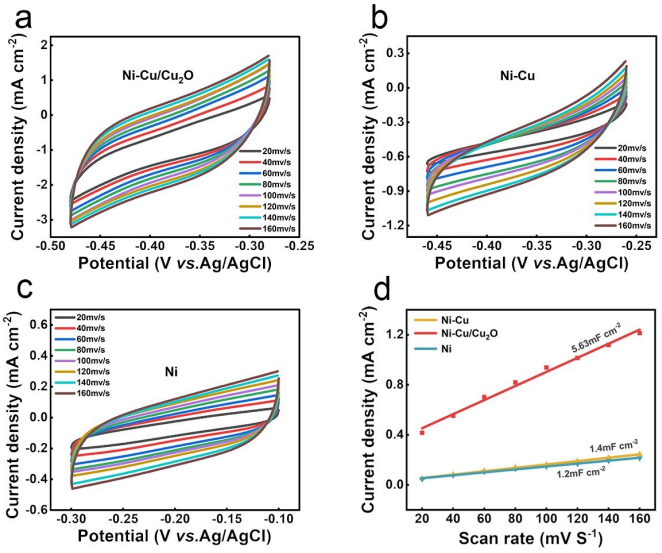

Fig. S16 (a-c) CV spectra of different samples at different scanning rate. (d) Double-layer capacitance (C_{dl}).

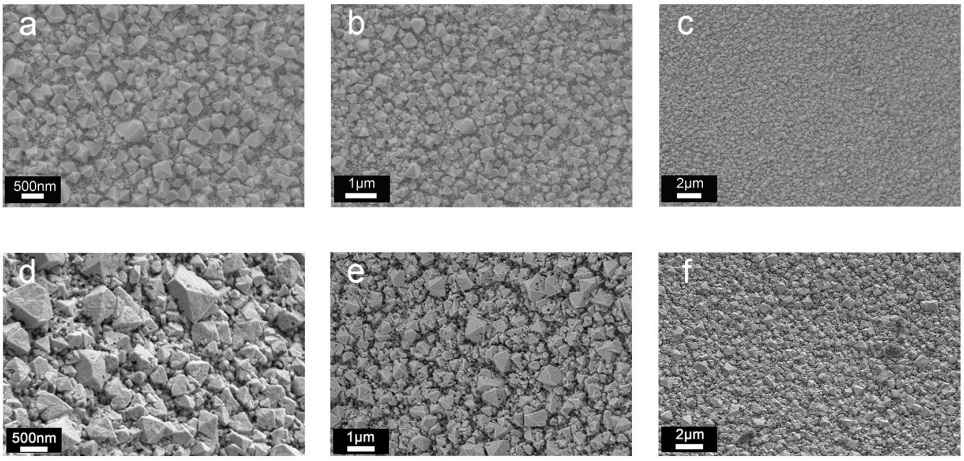

Fig. S17 (a-c) SEM images of Ni-Cu/Cu_2O at different magnification before 6 cycles of testing. (d-f) SEM images of Ni-Cu/Cu_2O at different magnification after 6 cycles of testing.

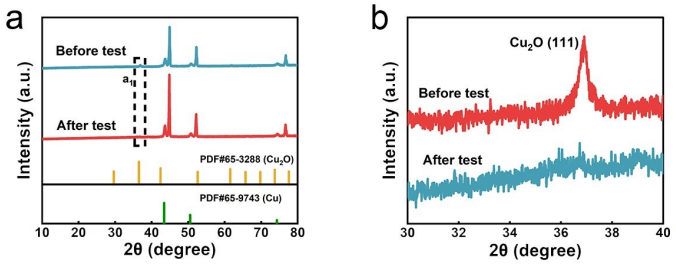

Fig. S18 XRD patterns of Ni-Cu/Cu_2O before and after 6 i-t cycles.

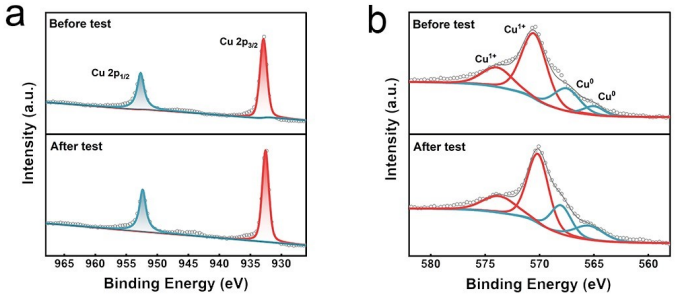

Fig. S19 Valence characterization of Ni-Cu/Cu_2O before and after after 6 times of i-t test. (a) The Cu 2p XPS spectra. (b) The Cu LMM XPS spectra.

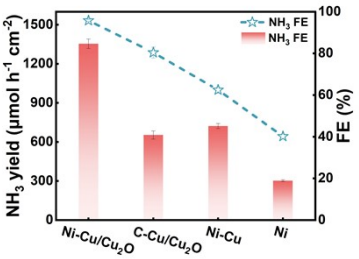

Fig. S20 The Faraday efficiency and NH_3 yield of Ni-Cu/Cu_2O, C-Cu/Cu_2O, Ni-Cu and Ni catalysts at -1.1 V (*vs*. RHE).

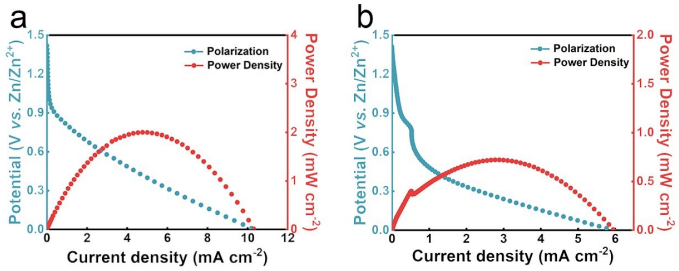

Fig. S21 Discharging curves and the resulted power density curve of (a) Ni-Cu and (b) Ni based Zn-NO_3^- battery.

Supporting Tables

Table S1 Comparison of FE and yield of ammonia by eNitRR.

Catalysts	NH_3 FE	NH_3 Yield	Ref.
Ni-Cu/Cu_2O	**95.8%**	**1354 μmol h^{-1} cm^{-2}**	**This work**
CuO/CF	80%	292 μmol h^{-1} cm^{-2}	[12]
$Cu_{2+1}O/Mn_3O_4$/CF	92.4%	210 μmol h^{-1} cm^{-2}	[13]
CoO-CuO_X	92.1%	510 μmol h^{-1} cm^{-2}	[14]
CoO/Cu foam	96.7%	253 μmol h^{-1} cm^{-2}	[15]
$Co_yNi_{1-y}(OH)_2$	94.9%	1176 μmol h^{-1} cm^{-2}	[16]
$Cu_{50}Ni_{50}$[a]	88%	584 μmol h^{-1} cm^{-2}	[17]
CuCl-BEF	44.7%	107.1 μmol h^{-1} cm^{-2}	[18]
Ni_{35}/NC-sd	99%	70.6 μmol h^{-1} cm^{-2}	[19]
CuCoSP	90.6%	1170 μmol h^{-1} cm^{-2}	[20]
CuO@PAN	93.88%	213 μmol h^{-1} cm^{-2}	[21]
$NiCo_2O_4$/CC	90%	973.2 μmol h^{-1} cm^{-2}	[22]
CuO	80%	292 μmol h^{-1} cm^{-2}	[23]
Ru/β-Co(OH)2	98.4%	1150 μmol h^{-1} cm^{-2}	[24]
Fe_2TiO_5	87.6%	730 μmol h^{-1} cm^{-2}	[25]
Fe/Cu	96.68%	1080 μmol h^{-1} cm^{-2}	[26]
a-RuO_2	97.46%	115.8 μmol h^{-1} cm^{-2}	[2]

Supporting References

1 B. Ravel and M. Newville, ATHENA, ARTEMIS, HEPHAESTUS: data analysis for X-ray absorption spectroscopy using IFEFFIT, *Journal of Synchrotron Radiation*, 2005, **12**, 537-541.

2 Y. Wang, H. Li, W. Zhou, X. Zhang, B. Zhang and Y. Yu, Structurally Disordered RuO2 Nanosheets with Rich Oxygen Vacancies for Enhanced Nitrate Electroreduction to Ammonia, *Angew. Chem. Int. Ed.*, 2022, **61**, e202202604.

3 Y. Gao, K. Huang, C. Yan, S. Li, H. Zhang, L. Cheng and F. Huang, Interfacial engineering of Cu–Fe2O3 nanotube arrays with built-in electric field and oxygen vacancies for boosting the electrocatalytic reduction of nitrates, *Materials Advances*, 2022, **3**, 7107-7115.

4 Y. Wang, Y. Yu, R. Jia, C. Zhang and B. Zhang, Electrochemical synthesis of nitric acid from air and ammonia through waste utilization, *Nat. Sci. Rev.*, 2019, **6**, 730-738.

5 G. Kresse and J. Hafner, Ab initio molecular dynamics for liquid metals, *Phys. Rev. B*, 1993, **47**, 558.

6 G. Kresse and J. Hafner, Ab initio molecular-dynamics simulation of the liquid-metal-amorphous-semiconductor transition in germanium, *Phys. Rev. B*, 1994, **49**, 14251.

7 n. Perdew, n. Burke and n. Ernzerhof, Generalized Gradient Approximation Made Simple, *Phys. Rev. Lett.*, 1996, **77**, 3865.

8 E. Torres and T. P. Kaloni, Projector augmented-wave pseudopotentials for uranium-based compounds, *Comput. Mater. Sci.*, 2020, **171**, 109237.

9 M. Engel, M. Marsman, C. Franchini and G. Kresse, Electron-phonon interactions using the projector augmented-wave method and Wannier functions, *Phys. Rev. B*, 2020, **101**, 184302.

10 J. K. Nørskov, J. Rossmeisl, A. Logadottir, L. Lindqvist, J. R. Kitchin, T. Bligaard and H. Jónsson, Origin of the Overpotential for Oxygen Reduction at a Fuel-Cell Cathode, *J. Phys. Chem. B*, 2004, **108**, 17886-17892.

11 L. I. Bendavid and E. A. Carter, CO2 Adsorption on Cu2O(111): A DFT+U and DFT-D Study, *J. Phys. Chem. C*, 2013, **117**, 26048-26059.

12 L. Fang, S. Wang, C. Song, S. Lu, X. Yang, X. Qi and H. Liu, Boosting nitrate electroreduction to ammonia via in situ generated stacking faults in oxide-derived copper, *Chem. Eng. J.*, 2022, **446**, 137341.

13 W. Jung, J. Jeong, Y. Chae, W. H. Lee, Y.-J. Ko, K. H. Chae, H.-s. Oh, U. Lee, D. K. Lee, B. K.

Min, H. Shin, Y. J. Hwang and D. H. Won, Synergistic bimetallic CuPd oxide alloy electrocatalyst for ammonia production from the electrochemical nitrate reaction, *J. Mater. Chem. A*, 2022, **10**, 23760-23769.

14 Y. Tang, S. Liu, C. Guo, Y. Liu and Z. Tang, Constructing a CoO–CuOx heterostructure for efficient electrochemical reduction of nitrate to ammonia, *Sustainable Energy Fuels*, 2023, **7**, 5039-5045.

15 W. Fu, Y. Du, J. Jing, C. Fu and M. Zhou, Highly selective nitrate reduction to ammonia on CoO/Cu foam via constructing interfacial electric field to tune adsorption of reactants, *Appl. Catal. B Environ.*, 2022, **324**, 122201.

16 L. Qiao, D. Liu, A. Zhu, J. Feng, P. Zhou, C. Liu, K. W. Ng and H. Pan, Nickel-facilitated in-situ surface reconstruction on spinel Co3O4 for enhanced electrochemical nitrate reduction to ammonia, *Appl. Catal. B Environ.*, 2023, **340**, 123219.

17. Y. Bu, C. Wang, W. Zhang, X. Yang, J. Ding and G. Gao, Electrical Pulse-Driven Periodic Self-Repair of Cu-Ni Tandem Catalyst for Efficient Ammonia Synthesis from Nitrate, *Angew. Chem. Int. Ed.*, 2023, **135**, e202217337.

18. W. J. Sun, H. Q. Ji, L. X. Li, H. Y. Zhang, Z. K. Wang, J. H. He and J. M. Lu, Built-in Electric Field Triggered Interfacial Accumulation Effect for Efficient Nitrate Removal at Ultra-Low Concentration and Electroreduction to Ammonia, *Angew. Chem. Int. Ed.*, 2021, **133**, 23115-23121.

19. P. Gao, Z. H. Xue, S. N. Zhang, D. Xu, G. Y. Zhai, Q. Y. Li, J. S. Chen and X. H. Li, Schottky Barrier-Induced Surface Electric Field Boosts Universal Reduction of NOx− in Water to Ammonia, *Angew. Chem. Int. Ed.*, 2021, **133**, 20879-20884.

20. W. He, J. Zhang, S. Dieckhöfer, S. Varhade, A. C. Brix, A. Lielpetere, S. Seisel, J. R. C. Junqueira and W. Schuhmann, Splicing the active phases of copper/cobalt-based catalysts achieves high-rate tandem electroreduction of nitrate to ammonia, *Nat. Commun.*, 2022, **13**, 1129.

21. Y. Xu, Y. Wen, T. Ren, H. Yu, K. Deng, Z. Wang, X. Li, L. Wang and H. Wang, Engineering the surface chemical microenvironment over CuO nanowire arrays by polyaniline modification for efficient ammonia electrosynthesis from nitrate, *Appl. Catal. B Environ.*, 2022, **320**, 121981.

22. Q. Liu, L. Xie, J. Liang, Y. Ren, Y. Wang, L. Zhang, L. Yue, T. Li, Y. Luo, N. Li, B. Tang, Y. Liu, S. Gao, A. A. Alshehri, I. Shakir, P. O. Agboola, Q. Kong, Q. Wang, D. Ma and X. Sun, Ambient Ammonia Synthesis via Electrochemical Reduction of Nitrate Enabled by NiCo2O4

Nanowire Array, *Small*, 2022, **18**, 2106961.

23. R. Daiyan, T. Tran-Phu, P. Kumar, K. Iputera, Z. Tong, J. Leverett, M. H. A. Khan, A. Asghar Esmailpour, A. Jalili, M. Lim, A. Tricoli, R.-S. Liu, X. Lu, E. Lovell and R. Amal, Nitrate reduction to ammonium: from CuO defect engineering to waste NOx-to-NH3 economic feasibility, *Energ. Environ. Sci.*, 2021, **14**, 3588-3598.

24. W. Zhu, F. Yao, Q. Wu, Q. Jiang, J. Wang, Z. Wang and H. Liang, Weakened d–p orbital hybridization in in situ reconstructed Ru/β-Co(OH)2 heterointerfaces for accelerated ammonia electrosynthesis from nitrates, *Energ. Environ. Sci.*, 2023, **16**, 2483-2493.

25. H. Du, H. Guo, K. Wang, X. Du, B. A. Beshiwork, S. Sun, Y. Luo, Q. Liu, T. Li and X. Sun, Durable Electrocatalytic Reduction of Nitrate to Ammonia over Defective Pseudobrookite Fe2TiO5 Nanofibers with Abundant Oxygen Vacancies, *Angew. Chem. Int. Ed.*, 2022, **62**, e202215782.

26. S. Zhang, J. Wu, M. Zheng, X. Jin, Z. Shen, Z. Li, Y. Wang, Q. Wang, X. Wang, H. Wei, J. Zhang, P. Wang, S. Zhang, L. Yu, L. Dong, Q. Zhu, H. Zhang and J. Lu, Fe/Cu diatomic catalysts for electrochemical nitrate reduction to ammonia, *Nat. Commun.*, 2023, **14**, 3634.